

# Spectroscopy of four metal-poor galaxies beyond redshift ten

Emma Curtis-Lake<sup>1\*</sup>, Stefano Carniani<sup>2†</sup>, Alex Cameron<sup>3</sup>, Stephane Charlot<sup>4</sup>, Peter Jakobsen<sup>5,6</sup>, Roberto Maiolino<sup>7,8,9</sup>, Andrew Bunker<sup>3</sup>, Joris Witstok<sup>7,8</sup>, Renske Smit<sup>10</sup>, Jacopo Chevallard<sup>3</sup>, Chris Willott<sup>11</sup>, Pierre Ferruit<sup>12</sup>, Santiago Arribas<sup>13</sup>, Nina Bonaventura<sup>5,6</sup>, Mirko Curti<sup>7,8</sup>, Francesco D'Eugenio<sup>7,8</sup>, Marijn Franx<sup>14</sup>, Giovanna Giardino<sup>15</sup>, Tobias J. Looser<sup>7,8</sup>, Nora Lützgendorf<sup>16</sup>, Michael V. Maseda<sup>17</sup>, Tim Rawle<sup>16</sup>, Hans-Walter Rix<sup>18</sup>, Bruno Rodriguez del Pino<sup>13</sup>, Hannah Übler<sup>7,8</sup>, Marco Sirianni<sup>16</sup>, Alan Dressler<sup>19</sup>, Eiichi Egami<sup>20</sup>, Daniel J. Eisenstein<sup>21</sup>, Ryan Endsley<sup>22</sup>, Kevin Hainline<sup>20</sup>, Ryan Hausen<sup>23</sup>, Benjamin D. Johnson<sup>21</sup>, Marcia Rieke<sup>20</sup>, Brant Robertson<sup>24</sup>, Irene Shivaie<sup>20</sup>, Daniel P. Stark<sup>20</sup>, Sandro Tacchella<sup>7,8</sup>, Christina C. Williams<sup>25</sup>, Christopher N. A. Willmer<sup>20</sup>, Rachana Bhatawdekar<sup>26</sup>, Rebecca Bowler<sup>27</sup>, Kristan Boyett<sup>28,29</sup>, Zuyi Chen<sup>20</sup>, Anna de Graaff<sup>18</sup>, Jakob M. Helton<sup>20</sup>, Raphael E. Hviding<sup>20</sup>, Gareth C. Jones<sup>3</sup>, Nimisha Kumari<sup>30</sup>, Jianwei Lyu<sup>20</sup>, Erica Nelson<sup>31</sup>, Michele Perna<sup>18</sup>, Lester Sandles<sup>7,8</sup>, Aayush Saxena<sup>3,9</sup>, Katherine A. Suess<sup>24,32</sup>, Fengwu Sun<sup>20</sup>, Michael W. Topping<sup>20</sup>, Imaan E. B. Wallace<sup>3</sup> and Lily Whitler<sup>20</sup>

<sup>1\*</sup>Centre for Astrophysics Research, Department of Physics, Astronomy and Mathematics, University of Hertfordshire, Hatfield AL10 9AB, UK.

<sup>2</sup>Scuola Normale Superiore, Piazza dei Cavalieri 7, I-56126 Pisa, Italy.

<sup>3</sup>Department of Physics, University of Oxford, Denys Wilkinson Building, Keble Road, Oxford OX1 3RH, UK.

- <sup>4</sup>Sorbonne Université, UPMC-CNRS, UMR7095, Institut d'Astrophysique de Paris, F-75014 Paris, France.
- <sup>5</sup>Cosmic Dawn Center (DAWN), Copenhagen, Denmark.
- <sup>6</sup>Niels Bohr Institute, University of Copenhagen, Jagtvej 128, DK-2200, Copenhagen, Denmark.
- <sup>7</sup>Kavli Institute for Cosmology, University of Cambridge, Madingley Road, Cambridge, CB3 0HA, UK.
- <sup>8</sup>Cavendish Laboratory - Astrophysics Group, University of Cambridge, 19 JJ Thomson Avenue, Cambridge, CB3 0HE, UK.
- <sup>9</sup>Department of Physics and Astronomy, University College London, Gower Street, London WC1E 6BT, UK.
- <sup>10</sup>Astrophysics Research Institute, Liverpool John Moores University, 146 Brownlow Hill, Liverpool L3 5RF, UK.
- <sup>11</sup>NRC Herzberg, 5071 West Saanich Rd, Victoria, BC V9E 2E7, Canada.
- <sup>12</sup>European Space Agency, European Space Astronomy Centre, Madrid, Spain.
- <sup>13</sup>Centro de Astrobiología (CAB), CSIC-INTA, Cra. de Ajalvir Km. 4, 28850- Torrejón de Ardoz, Madrid, Spain.
- <sup>14</sup>Leiden Observatory, Leiden University, P.O. Box 9513, NL-2300 RA Leiden, Netherlands..
- <sup>15</sup>ATG Europe for the European Space Agency, ESTEC, Noordwijk, The Netherlands.
- <sup>16</sup>European Space Agency (ESA), ESA Office, STScI, Baltimore, MD 21218, USA.
- <sup>17</sup>Department of Astronomy, University of Wisconsin-Madison, 475 N. Charter St., Madison, WI 53706, USA.
- <sup>18</sup>Max-Planck-Institut für Astronomie, Königstuhl 17, D-69117, Heidelberg, Germany.
- <sup>19</sup>The Observatories of the Carnegie Institution for Science, 813 Santa Barbara St., Pasadena, CA 91101, USA.
- <sup>20</sup>Steward Observatory University of Arizona 933 N. Cherry Avenue ,Tucson, AZ 85721, USA.
- <sup>21</sup>Center for Astrophysics || Harvard & Smithsonian, 60 Garden St., Cambridge, MA 02138, USA.
- <sup>22</sup>Department of Astronomy, University of Texas, Austin, TX 78712, USA.
- <sup>23</sup>Department of Physics and Astronomy, The Johns Hopkins University, 3400 N. Charles St., Baltimore, MD 21218, USA.

<sup>24</sup>Department of Astronomy and Astrophysics University of California, Santa Cruz, 1156 High Street, Santa Cruz, CA 96054, USA.

<sup>25</sup>NSF's National Optical-Infrared Astronomy Research Laboratory, 950 North Cherry Avenue, Tucson, AZ 85719, USA.

<sup>26</sup>European Space Agency, ESA/ESTEC, Keplerlaan 1, 2201 AZ Noordwijk, NL.

<sup>27</sup>Jodrell Bank Centre for Astrophysics, Department of Physics and Astronomy, School of Natural Sciences, The University of Manchester, Manchester, M13 9PL, UK.

<sup>28</sup>School of Physics, University of Melbourne, Parkville 3010, VIC, Australia.

<sup>29</sup>ARC Centre of Excellence for All Sky Astrophysics in 3 Dimensions (ASTRO 3D), Australia.

<sup>30</sup>AURA for European Space Agency, Space Telescope Science Institute, 3700 San Martin Drive, Baltimore, MD 21218, USA.

<sup>31</sup>Department for Astrophysical and Planetary Science, University of Colorado, Boulder, CO 80309, USA.

<sup>32</sup>Kavli Institute for Particle Astrophysics and Cosmology and Department of Physics, Stanford University, Stanford, CA 94305, USA.

\*Corresponding author(s). E-mail(s): [e.curtis-lake@herts.ac.uk](mailto:e.curtis-lake@herts.ac.uk);  
Contributing authors: [stefano.carniani@sns.it](mailto:stefano.carniani@sns.it);

†These authors contributed equally to this work.

## Abstract

Finding and characterising the first galaxies that illuminated the early Universe at cosmic dawn is pivotal to understand the physical conditions and the processes that led to the formation of the first stars [1]. In the first few months of operations, imaging from the James Webb Space Telescope (JWST) has been used to identify tens of candidates of galaxies at redshift ( $z$ ) greater than 10 [2–9], less than 450 million years after the Big Bang. However, none of such candidates has yet been confirmed spectroscopically, leaving open the possibility that they are actually low-redshift interlopers. Here we present spectroscopic confirmation and analysis of four galaxies unambiguously detected at redshift  $10.3 \leq z \leq 13.2$ , previously selected from NIRC*am* imaging [10]. The spectra reveal that these primeval galaxies are extremely metal poor, have masses between  $10^7$  and a few times  $10^8$  solar masses, and young ages.

**The damping wings that shape the continuum close to the Lyman edge are consistent with a fully neutral intergalactic medium at this epoch. These findings demonstrate the rapid emergence of the first generations of galaxies at cosmic dawn.**

**Keywords:** keyword1, Keyword2, Keyword3, Keyword4

The opening act of galaxy formation in the first billion years after the Big Bang sets in motion crucial themes for the rest of the play. Galaxies forming at these times may be the seeds of the much more massive and mature galaxies in the local Universe. Theoretical models and cosmological simulations differ greatly in their predictions of the physical properties and abundance of the first galaxies. The theoretical pictures depend strongly on assumptions about the physical processes at play in the early universe, such as: gas cooling and fragmentation in primordial clouds; the feedback effects from first stars and supernova explosions that subsequently enrich the surrounding medium; and early merging, assembly and accretion histories of galaxies [e.g. 1, 11–16]. The abundance and mass distribution of the first galaxies are also tightly connected to early structure formation. Therefore, the detection and characterisation of these early galaxies is key to test different models and theories.

This is one of the primary goals for which *JWST* was designed. The first few months of *JWST* imaging have already yielded a large number of candidate galaxies at  $z > 10$  [e.g. 2–9]. However, the redshift estimates of these candidates have so far been based on their broad-band spectral energy distributions (SEDs), and it cannot be ruled out that such candidates are actually lower redshift galaxies.

High-redshift galaxies often have distinctive spectra in the ultraviolet, in which the blue spectrum produced by hot massive stars is abruptly cut off below the Lyman-limit at  $912\text{\AA}$  (rest-frame) by the absorption of the light by neutral Hydrogen in the intergalactic medium (IGM). At the highest redshifts ( $z \gtrsim 6$ ), the inter-galactic neutral Hydrogen leads to almost complete absorption at wavelengths below  $\text{Ly}\alpha$  at  $1216\text{\AA}$ . Observationally, this translates to a ‘dropout’, i.e., a lack of detection in bands blue-ward of  $(1+z) \times 1216\text{\AA}$  but flux red-ward of the same wavelength [17–19]. However, galaxies with peculiar properties may mimic high-redshift galaxies [e.g., a combination of dust reddening and nebular lines as in 20]. Therefore, spectroscopic observations are the only method to determine secure redshifts, either via the detection of the (redshifted) nebular lines, or via the unambiguous detection of the sharp continuum cutoff at  $(1+z) \times 1216\text{\AA}$ .

We report here the first deep spectroscopic observations with *NIRSpec* [21] on *JWST*, which provides confirmation of four candidates at  $z > 10$  and extensive characterisation of their physical properties. These candidates were photometrically identified as part of the *JWST* Advanced Deep Extragalactic Survey (JADES), a joint guaranteed time project of the *NIRCam* and

NIRSpec instrument teams. The identification and photometric study of these candidates, based on Hubble Space Telescope (*HST*) and NIRC*am* data [22], is described in a companion paper [10]. We specifically focus here on a pointing in the Hubble Ultra Deep Field (in the GOODS-South area), in which we have taken multi-object spectroscopy of 253 galaxies observed simultaneously with NIRSpec's configurable array of microshutters. We report here on observations taken with the prism spectral configuration (spectral range 0.6-5.3  $\mu\text{m}$ , resolving power  $R \sim 100$ ) with exposure times ranging from 9.3 to 28 hours (see Methods for details on the observing strategy).

The JADES spectroscopic observations reach an unprecedented sensitivity of 28.4 magnitudes (AB) at  $5\sigma$  per resolution element on the continuum at 2.5  $\mu\text{m}$ . We note that the NIRSpec prism is extremely well-suited for the redshift confirmation of high- $z$  candidates, with low spectral resolution and high sensitivity at short wavelengths where we are searching for a spectral break (around 1-2  $\mu\text{m}$ ), and higher resolution in the 3-5  $\mu\text{m}$  region, where we are searching for narrow spectral lines.

The focus of this paper is on four of these spectroscopic targets. Two of these are  $z > 12$  galaxy candidates selected from NIRC*am* imaging [10], based on a clear lack of F150W flux. Two others are  $z > 10$  candidates based on their *HST* IR photometry. We defer to description of the other targets in this deep pointing to a future publication. All candidates are faint, with F200W magnitudes fainter than 28 (AB), and hence entirely out of reach for any spectroscopic facility before *JWST*. More details on the selection and photometric properties of these candidates are provided in the companion paper [10].

In Figure 1 we show the 1D and 2D spectra of these four galaxies. All show a clear detection of a blue continuum that drops off sharply in a manner consistent with a  $z > 10$  Lyman dropout. Specifically, in Figure 1, we show the redshift derived from the position of the spectral break, taken to be at the wavelength of Ly $\alpha$  at 1215.67Å. These redshifts are reported in Table 1 and were derived with full spectral fitting over the entire redshift range, with each object consistently showing peaks in the posterior probability distribution only at high redshifts. We note that both the spectra and the photometry from ref. [10] agree on the wavelength of the break. This provides further compelling confirmation of the redshift.

We tested whether the observed breaks might be produced by the Balmer (or 4000Å) break in the stellar continuum associated with evolved stellar populations in galaxies at  $z \sim 3$ , and we show that this possibility is excluded with high confidence (see Methods section).

One of the galaxies, JADES-GS-z11-0, has been debated in the literature. It was first identified in [23] as a potential  $z \sim 10$  galaxy. In the UDF12 survey [24, 25], deep *Hubble* imaging revealed the object drops out in JH<sub>140</sub> band imaging. This left two possibilities, either the source was at very high redshift [ $z \sim 11.9$  24], or was low redshift, with a high equivalent width emission line producing the flux in the *Hubble* H<sub>160</sub> image. In fact, [26] found indication of

a possible emission line in spectroscopic follow-up supporting the latter explanation. We do not confirm this line emission in our NIRSpec spectroscopy, and the NIRC*am* imaging present in ref. [10] shows that the continuum emission extends to longer wavelengths, which is consistent with the spectrum shown here [see also 27]. Therefore, this galaxy is indeed at high redshift, and not a low-redshift contaminant.

**Table 1** Exposure times, redshifts (derived both from assuming the spectral break is at exactly 1215.67Å and accounting for the damping wing from a fully neutral IGM), upper limits on emission line equivalent widths (rest frame) for the CIII]λ1907, 1909 and HeIIλ1640 lines, the 2σ lower limits on the strength of the observed spectral breaks (measurements described in Methods 2), UV absolute magnitude,  $M_{UV}$ , and UV-slope,  $\beta$  (measured directly from the spectra, see Methods 2.3) and BEAGLE-derived physical properties for the four objects. For the BEAGLE-derived properties we report posterior medians and limits in the 1σ credible region.

JADES-ID	GS-z10-0	GS-z11-0	GS-z12-0	GS-z13-0
Exposure time (s)	67225.6	100838.0	67225.6	33612.8
$z_{1216}^*$	$10.38^{+0.07}_{-0.06}$	$11.58^{+0.05}_{-0.05}$	$12.63^{+0.24}_{-0.08}$	$13.20^{+0.04}_{-0.07}$
$z_{\text{HI}}^\dagger$	$10.37^{+0.03}_{-0.02}$	$11.48^{+0.03}_{-0.08}$	$12.60^{+0.04}_{-0.05}$	$13.17^{+0.16}_{-0.15}$
EW(CIII)]/Å 2σ	< 13.8	< 5.9	< 12.4	< 15.2
EW(HeII)/Å 2σ	< 14.8	< 6.0	< 13.5	< 15.4
2σ break strength	> 2.04	> 6.85	> 2.48	> 2.79
$M_{UV}$	$-18.61 \pm 0.10$	$-19.34 \pm 0.05$	$-18.23 \pm 0.16$	$-18.73 \pm 0.06^\ddagger$
$\beta$	$-2.49 \pm 0.22$	$-2.18 \pm 0.09$	$-1.84 \pm 0.19$	$-2.37 \pm 0.12^\ddagger$
$\log(M/M_\odot)$	$7.58^{+0.19}_{-0.20}$	$8.67^{+0.08}_{-0.13}$	$7.64^{+0.66}_{-0.39}$	$7.95^{+0.19}_{-0.29}$
$\Psi/M_\odot \text{ yr}^{-1}\P$	$1.1^{+0.19}_{-0.16}$	$2.2^{+0.28}_{-0.22}$	$1.8^{+0.54}_{-0.43}$	$1.36^{+0.31}_{-0.23}$
$\log(t/\text{yr})^\parallel$	$7.54^{+0.25}_{-0.24}$	$8.35^{+0.08}_{-0.17}$	$7.36^{+0.75}_{-0.59}$	$7.84^{+0.23}_{-0.36}$
$\log(Z/Z_\odot)^{**}$	$-1.91^{+0.25}_{-0.20}$	$-1.87^{+0.28}_{-0.18}$	$-1.44^{+0.23}_{-0.22}$	$-1.69^{+0.28}_{-0.31}$
$\hat{\tau}_V^{\dagger\dagger}$	$0.05^{+0.03}_{-0.02}$	$0.18^{+0.06}_{-0.06}$	$0.17^{+0.20}_{-0.09}$	$0.10^{+0.08}_{-0.05}$
$\xi_{\text{ion}}^\S$	$25.46^{+0.07}_{-0.07}$	$25.43^{+0.06}_{-0.06}$	$25.72^{+0.16}_{-0.19}$	$25.47^{+0.10}_{-0.09}$

\*The redshift based on the spectral break being at 1215.67Å †The redshift accounting for a fully neutral IGM ( $x_{\text{HI}} = 1$ ) following the method outlined in Methods 2.1. ‡For JADES-GS-z13-0, we report  $\beta$  and  $M_{UV}$  derived from the BEAGLE fitting, since we know this object to be on the edge of the shutter, and hence incorporate NIRC*am* photometry in the fitting to this one object to account for slit-losses (see Methods 3). ¶ $\Psi$  is the star formation rate. †† $t$  is age of the oldest stars, or maximum stellar age. \*\* $Z$  is the metallicity. ††† $\hat{\tau}_V$  is the effective V-band attenuation optical depth. §The production rate of H-ionizing photons per unit monochromatic UV luminosity.

The continua appear mostly featureless, with the possible exceptions of JADES-GS-z10-0, which shows a tentative emission line at  $\sim 1.44 \mu\text{m}$  which may indicate Ly $\alpha$  emission, and JADES-GS-z12-0, which shows another tentative feature at  $\sim 5.23 \mu\text{m}$ , which could be interpreted as [Ne III]λ3869 emission at  $z = 12.52$ . However, both features are only marginally detected, and we are still assessing whether these very faint and localized features are astrophysical. They will be assessed and explored more in detail in forthcoming papers and not discussed further here.

Leaving aside these two features, we report the  $2\sigma$  upper limits on the equivalent widths (EW) of He II  $\lambda 1640$  and C III]  $\lambda 1907, 1909$  in Table 1 (see Methods 2.2 for details of the measurements). These lines are important as C III]  $\lambda 1907, 1909$  is often the strongest line in the rest-frame UV of low-metallicity galaxies [e.g. 28] and strong He II  $\lambda 1640$  is expected in galaxies of zero metallicity. Nearby metal poor galaxies ( $Z/Z_{\odot} \lesssim 0.1$ ) show EWs of C III]  $\lambda 1907, 1909$  spanning  $\sim 6 - 16 \text{ \AA}$  [28, 29], making our measured limits not yet particularly constraining. The limits on EW(He II  $\lambda 1640$ ) are above the actually measured equivalent widths in these studies, and comparable or higher than the majority of objects in the MUSE-selected sample spanning  $2 \lesssim z \lesssim 4$  of [30].

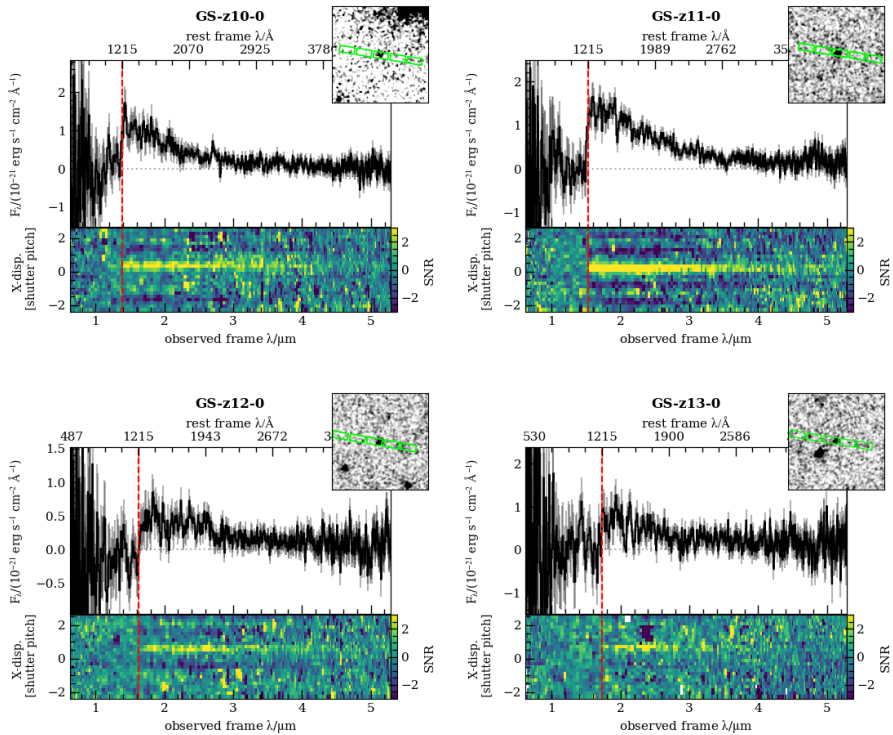


**Fig. 1** NIRSpec prism  $R \sim 100$  spectra for the four  $z > 10$  galaxies targeted for the first deep spectroscopic pointing of the JADES survey, JADES-GS-z10-0, JADES-GS-z11-0, JADES-GS-z12-0 and JADES-GS-z13-0. For each galaxy we display the 1D spectrum and associated uncertainties. In the bottom panel we show the 2D signal-to-noise ratio plot. The 2D plot is binned over four pixels in the wavelength direction to better show the contrast across the break. The inset panel in the top right-hand corner shows the the NIRCам F444W filter image with the three nodding positions of the the NIRSpec micro-shutter 3-slitlet array shown in green. The red dashed line shows  $1215.67 \text{ \AA}$  at the observed redshift  $z_{1216}$ .

Spectral fitting with BEAGLE [Bayesian Analysis of Galaxy sEds, 31] with a constant star formation history (SFH) provides constraints on the young stellar populations within these galaxies (see Methods section 3 for more details). These fits are illustrated in Extended Data Figures 2–5. We find extremely low metallicities consistent with just a few percent of solar, while star formation rates are moderate, at just a few solar masses a year. Metallicity could not be constrained from the NIRC*am* photometry alone [10]. We caution that total star formation rates and stellar masses require slit-loss corrections which can be best derived from NIRC*am* photometry if the objects are extended, or on the edge of the shutter. The fitted parameters are given in Table 1.

We investigate whether the lack of detectable line emission requires a large escape fraction of ionising photons and find no strong dependence of the physical properties, nor strong constraints on the escape fraction. We do note, however, that JADES-GS-z11-0 has a solution with low ages and high escape fraction with marginally higher metallicity, though the upper  $1\sigma$  limit is still  $\sim 5\%$  solar metallicity (see Extended Data Table 3). In fact, at these extremely low metallicities, the rest-frame UV emission lines might be significantly weaker than those sometimes found in lower redshift samples with somewhat higher metallicities around  $\sim 10\%$  solar. However, another important factor is the age of the stellar populations, as strong UV emission lines have primarily been observed in galaxies with UV light dominated by very young stellar populations [ $\lesssim 10$  million years 28].

Two objects, JADES-GS-z11-0 and JADES-GS-z12-0 do indicate moderate levels of dust, albeit with large uncertainties (with V-band optical depth,  $\hat{\tau}_v = 0.18^{+0.06}_{-0.06}$  and  $\hat{\tau}_v = 0.2^{+0.16}_{-0.09}$ , respectively). Dust in such low metallicity systems would be physically hard to explain unless a low dust-to-gas ratio is coupled with large HI column densities. However, we note that recent models do expect significant dust production by the first generations of stars [e.g. 12, 32]. When fit without any dust, JADES-GS-z11-0 required a higher metallicity (up to 40% solar at  $1\sigma$ ), while the JADES-GS-z12-0 data yield similar parameter constraints to those reported in Table 1.

The spectra do not provide strong constraints red-ward of the Balmer-break, the longest rest-frame wavelength probed being  $\sim 3660 - 4350\text{\AA}$ . We see no evidence for strong Balmer breaks in these objects, but the S/N in this region of the spectra are low. Correspondingly, the constraints on stellar age and stellar mass (sensitive to the Balmer-break strength) are broad. The ages range from  $\sim 5$  to 230 Myrs, and stellar masses range from  $\sim 2 \times 10^6 M_\odot$  to  $460 \times 10^6 M_\odot$ , though the constraints on these parameters are weak, and highly sensitive to the prior regarding the time history of the star formation rate. The associated production rates of H-ionizing photons per unit monochromatic UV luminosity,  $\xi_{\text{ion}}$ , are similar to those measured in extreme star-forming regions in low-redshift, metal-poor galaxies [33].

We show the measured UV slopes ( $\beta$ ) vs. absolute magnitude at  $1500\text{\AA}$  ( $M_{\text{UV}}$ ) in Figure 2. We compare to other *JWST*-selected high-redshift candidate samples spanning photometric redshifts  $z \sim 7 - 16$  [9, 34, 35]. Our



measured slopes at such faint  $M_{UV}$  magnitudes are comparable to the other literature samples, suggesting little evolution at these epochs. Very blue UV slopes are used to search for extreme stellar populations at the earliest times [e.g. 36]. In this case, we find extreme stellar populations but the effect of the nebular recombination continuum is to redden the UV slopes [e.g. 35].

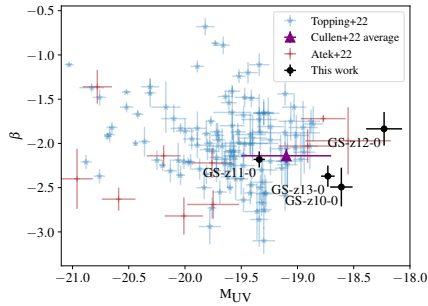


**Fig. 2** UV slope,  $\beta$ , as a function of absolute magnitude at  $1500\text{\AA}$ ,  $M_{UV}$ , as measured as described in Methods 2.3. These are compared to the measurements from photometrically selected high-redshift candidates. Specifically, the average  $\beta$  measured from objects spanning  $z \sim 8 - 15$  at similar  $M_{UV}$  from Cullen+22 [34], as well as a sample from Atek+22 [9] spanning  $z \sim 9 - 16$ , and also the sample presented in Topping+22 [35] (itself collated from the samples of [8, 37] and spanning  $z \sim 7 - 11$ ).

We find that the spectral breaks seen in the four objects reported here are less abrupt than those seen in galaxies at lower redshifts in our spectroscopic data set, and are consistent with a softening of the break by the Ly $\alpha$  damping wing caused by a fully neutral IGM. The redshift is sensitive to the form and existence of this damping wing, and we report the best-fit redshift for a fully neutral inter-galactic medium ( $x_{\text{HI}} = 1$ , where  $x_{\text{HI}}$  is the fraction of neutral Hydrogen) in Table 1. For the object with the highest S/N in the Ly $\alpha$  break region (JADES-GS-z11-0), we investigate the constraints we can place on the neutral Hydrogen fraction by first fixing the best-fit model for the stellar population. We then run BEAGLE varying only redshift and  $x_{\text{HI}}$ . The resulting fit to the spectral break, and the derived constraints are shown in Figure 3. The 2D posterior probability distribution function reported in the right-hand panel indicates that the constraints on  $x_{\text{HI}}$  are sensitive to the exact redshift of the source, and without emission line detections to pin down the systemic redshift we cannot provide strong constraints on  $x_{\text{HI}}$ . However, these spectra demonstrate that  $x_{\text{HI}}$  can be constrained from *JWST* R100 spectra at slightly lower redshifts from ‘normal’ star-forming galaxies.

To date the only constraints on the evolution of  $x_{\text{HI}}$  from damping wings is in luminous quasars at  $6 < z < 7.5$ . Damping wings are rarely observed at  $z < 7$ , but become more common in the small sample of known  $z > 7$  quasars, consistent with  $x_{\text{HI}} \sim 0.5$  at  $z = 7.3$  [38]. Whilst star-forming galaxies are less luminous than quasars, they have several advantages in being plentiful at

redshifts 7 to 9, provide an independent test of neutrality at higher redshifts. Finally galaxies do not have broad Ly $\alpha$  and N V $\lambda$ 1240 emission, using their spectra to measuring the damping wing may simplify the modelling [39].

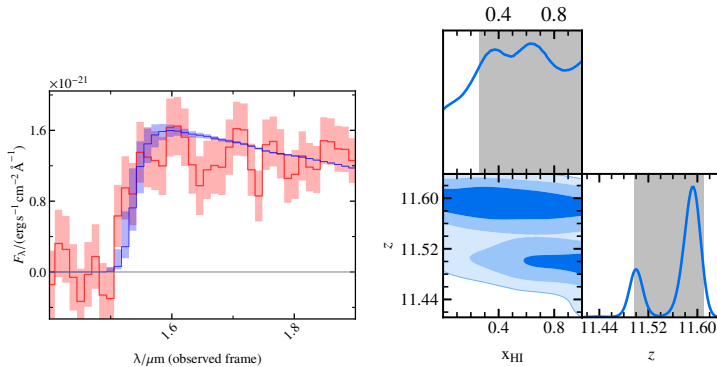


**Fig. 3** BEAGLE fit to the spectral break region of JADES-GS-z11-0 (left panel), while varying the fraction of neutral Hydrogen in the IGM,  $x_{\text{HI}}$ . The red line and shaded region shows the extracted spectrum and per-pixel uncertainties and the blue line and shaded region shows the range and median of the fitted models, respectively. The right-hand panel shows the 2D constraints on redshift and  $x_{\text{HI}}$ , which were varied in the fit while keeping all other physical properties constant (see text for details) For this test, we use a spectral extraction over 3 pixels that maximises the S/N in the region of the break. The shape of the damping wing is not sensitive to wavelength-dependent slit-losses introduced by such a small extraction box since the wing it extends over just tens of pixels.

We conclude by emphasizing that this is clearly a milestone result for the *JWST* mission, pushing the spectroscopic frontier to a markedly earlier epoch of galaxy formation. In addition to providing clear detections of the Lyman dropouts as high as  $z = 13.2$ , these JADES observations also show the power of spectroscopy to probe the physics of these galaxies and the IGM. Truly, this is just a starting point for the mission. JADES and other programmes have extensive amounts of spectroscopy approved for *JWST*-detected high-redshift candidates.

## Methods

### 1 NIRSpec observations and data reduction

The NIRSpec observations presented here are part of GTO program ID: 1210 (Principal Investigator: Lützgendorf) and were obtained between October 22 and 25, 2022. The program used a three-point nod pattern for background subtraction, as well as three small dithers with microshutter array (MSA) reconfigurations in order to improve spatial sampling, increase sensitivity and

flux accuracy, mitigate the impact of the detector gaps, and aid removal of cosmic rays.

Each dither pointing included four sequences of three nodded exposures each to build up signal-to-noise. Observations were carried out by using the disperser-filter combination PRISM/CLEAR, which covers the wavelength range between  $0.6 \mu\text{m}$  and  $5.3 \mu\text{m}$  and provides spectra with a spectral power of  $R \sim 100$  [21]. Each PRISM/CLEAR setup had two integrations of 19 groups, resulting in an exposure time of 8278 seconds for each sequence and of 33612 seconds for each dither pointing.

A total of 253 galaxies were observed over the three dither pointings. As the non-functioning shutters and rigid grid of the MSA prevents some slit locations from being used, some galaxies were not observed on all three pointings. More specifically, among the four sources presented in this paper, JADES-GS-z11-0 was observed in all three MSA dither pointings, JADES-GS-z10-0 and JADES-GS-z12-0 were present in two dither pointings, whereas JADES-GS-z13-0 was only observed in one dither pointing. The different resulting exposure times for each target are reported in Table 1.

Flux-calibrated 2D spectra and 1D spectral extractions have been produced using pipelines developed by the ESA NIRSpec Science Operations Team (SOT) and the NIRSpec GTO Team. We briefly outline here the main steps, while a more detailed description will be presented in a forthcoming NIRSpec/GTO collaboration paper. Most of the processing steps in the pipelines adopt the same algorithms included in the official STScI pipeline used to generate the MAST archive products [see Fig. 11 and section 4.3 of 40]. Initially, we processed the MOS raw data (i.e., level 1a data from the MAST archive) with the ramp-to-slope pipeline that estimates the count rate per pixel by using all unsaturated groups in the ramp. Ramp jumps due to cosmic rays are detected and rejected on the basis of the slope of the individual ramps. The ramp-to-slope pipeline also includes the following steps: saturation detection and flagging, master bias subtraction, reference pixel subtraction, linearity correction, dark subtraction, snowball artifact detection and correction, and count rate estimation [for more details see 40–43]. All the count-rate images were then processed using a data reduction pipeline including ESA NIRSpec SOT codes and NIRSpec GTO algorithms. The pipeline has 11 main steps: 1) identification of non-target galaxies intercepting the open shutters; 2) pixel-level background subtraction by combining the three nod exposures (excluding nods contaminated by non-target sources); 3) extraction of sub-images containing the spectral trace of each target and wavelength and spatial coordinate assignments to each pixel in the 2D maps; 4) pixel-to-pixel flat-field correction; 5) spectrograph optics and dispersers correction; 6) absolute flux calibration; 7) slit-losses correction; 8) rectification of the spectral trace; 9) extraction of 1D spectra; 10) combination of 1D spectra generated from each integration, nod, and pointing; 11) combination of 2D maps. The data processing workflow thus returns both a combined 1D and 2D spectrum for each target. We

stress however that the combined 1D spectra are not extracted from the combined 2D maps, but are the result of a weighted average of 1D spectra from all integrations. This process allowed us to mask the bad pixels indicated on the quality flags and to reject outlier pixels. Finally, we adopted an irregular wavelength grid for the 1D and 2D spectra to avoid oversampling of the line spread function at short wavelengths ( $\lambda \sim 1 \mu\text{m}$ ).

Given the compact size of our  $z > 10$  targets, we computed and applied slit-loss corrections, modelling galaxies as point-like sources, but taking into account the relative intra-shutter position of each source (each microshutter has an illuminated area of  $0.2'' \times 0.46''$ ). For each target we extracted the 1D spectra from two different apertures. One aperture was as large as the shutter size to recover all emission of the galaxy, while the second extraction was performed in an aperture of 3 pixels height (with NIRSpec spatial pixel scale of  $0.1''/\text{pixel}$ ) to maximise the signal-to-noise ratio of the final spectra.

For most uses of the extraction performed on a 3 pixel aperture, the measurements are performed over small wavelength ranges and further corrections for losses due to the smaller extraction box are not required. In the case of full spectral fitting we use the extraction over the 5 pixel aperture with one exception, JADES-GS-z13-0. In this case we mitigate the wavelength-dependent losses with simultaneous fitting to photometry (see Section 3).

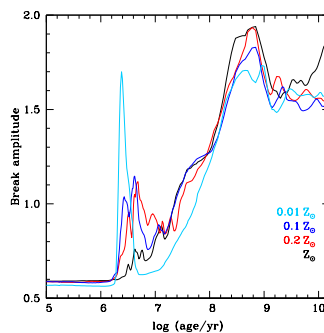
## 2 Empirical measurements

The central aspects of the astrophysical analysis of the spectra has been presented in the main part of the paper. Here we explore a few more issues that bolster the fidelity and robustness of our analysis.

### 2.1 Balmer break index

While the observed spectral breaks in the four objects presented are fully consistent with expectations for high-redshift galaxies, it is important to test the possibility that the observed breaks are Balmer breaks at lower redshift. We test this using empirical spectral indices. We adapt the classical Balmer break index definition [e.g. 44] and define the break amplitude as the ratio of  $f_\lambda$  in the rest-frame range  $3751 \text{ \AA} - 4198 \text{ \AA}$  to that in the range  $3145 \text{ \AA} - 3563 \text{ \AA}$ . This definition expands the spectral windows to include more spectral pixels and increase the signal-to-noise on the index. The number of spectral pixels range from 15 to 19 depending on the redshift. These measurements are taken from spectra extracted from 3 pixels, maximising the S/N. The effect of wavelength-dependent extraction losses should be minimal for this measurement as it extends over such a small wavelength range. When the lower spectral range yields a negative flux, we adopt the  $2\sigma$  upper flux limit instead. Additionally, to account for the noisy measurement of the (physically) positive-definite flux in the longer wavelength band we subtract  $1\sigma$  from the measured flux. This is a conservative upper-limit which we quote as a  $2\sigma$  upper limit in Table 1.

In Extended Data Figure 1 we show the evolution of the modified Balmer break index with age for single stellar population models at four different metallicities from  $0.01Z_{\odot}$  to  $1Z_{\odot}$ . The maximum value reached within 10 Gyr is less than 2.0. We report 2-sigma lower limits on the value of this index for each of our four targets in Table 1. For three of our targets, the lower limit on the amplitude of this index is greater than 2.4, suggesting that our observations cannot be reproduced by a Balmer break. For one object (GS-z10-0), we calculate a 2-sigma lower limit of 2.04, which is higher than the maximum reached by the single stellar populations in Extended Data Figure 1. Again, this suggests that the Balmer break solution is unlikely, although by a smaller margin than for the other three targets.



**Extended Data Fig. 1 | Balmer-break amplitude plotted against age for single stellar populations with metallicities  $0.01Z_{\odot}$ ,  $0.1Z_{\odot}$ ,  $0.2Z_{\odot}$ , and  $Z_{\odot}$  (as indicated), according to the models described in Section 3.** The break is defined as the ratio of the flux  $f_{\lambda}$  integrated over the rest-frame 3751–4198 Å wavelength range to that in the rest-frame 3145–3563 Å wavelength range. The peak at early ages for all metallicities arises from the onset or red supergiant stars, and that around  $6 \times 10^8$  yr from bright asymptotic-giant-branch stars.

## 2.2 Limits on possible emission lines

Apart from the possible detections of Ly $\alpha$  in JADES-GS-z10-0 and [Ne III] $\lambda$ 3869 in JADES-GS-z12-0 (which we will assess in future work), visual inspection of the 1D and 2D spectra did not show the presence of any emission lines above the level of the noise in any of the four targets. We derive upper limits to emission line fluxes and equivalent widths using the error spectrum output from the data reduction pipeline from the optimised S/N spectra extracted over 3 pixels. Our reduced spectra have an irregular wavelength grid, and we estimate that the line spread function of these PRISM spectra results

in unresolved emission lines that have FWHM of approximately 2-3 spectral pixels. Thus, to calculate our emission line limits, for the 3 spectral pixels centered on the expected centroid of the emission line at the calculated redshift, we sum the pixel errors in quadrature and multiply the result by the wavelength interval between pixels. This results in 1-sigma upper limits on line fluxes, which we convert to equivalent width limits by fitting a simple polynomial to the continuum of each object to get the level on the continuum and associated uncertainty. Table 1 reports 2-sigma upper limits on the equivalent widths of He II  $\lambda$ 1640 and C III  $\lambda$ 1907, 1909, while the full set of limits on rest-frame UV emission lines is given in Table 2.2.

**Extended Data Table 1** |  $2\sigma$  upper limits on the rest-frame equivalent widths (in Å) and observed line fluxes (in  $\text{erg s}^{-1} \text{cm}^{-2}$ ) of rest-frame UV emission lines.

JADES-ID	GS-z10-0	GS-z11-0	GS-z12-0	GS-z-12-0
EW(C III $\lambda$ 1907, 1909)	< 13.74	< 5.84	< 11.94	< 14.4
EW(He II $\lambda$ 4686)	< 14.80	< 5.98	< 12.84	< 14.52
EW(C IV $\lambda$ 1548)	< 13.92	< 6.08	< 12.98	< 14.20
EW(O III $\lambda$ 1661, 1666)	< 14.12	< 5.94	< 12.80	< 14.74
C III $\lambda$ 1907, 1909	< 8.43e-20	< 5.60e-20	< 4.88e-20	< 7.09e-20
He II $\lambda$ 4686	< 1.26e-19	< 8.08e-20	< 7.14e-20	< 1.01e-19
C IV $\lambda$ 1548	< 1.33e-19	< 9.23e-20	< 7.98e-20	< 1.11e-19
O III $\lambda$ 1661, 1666	< 1.17e-19	< 7.77e-20	< 6.92e-20	< 9.93e-20

### 2.3 $M_{UV}$ and UV slopes

The UV slope,  $\beta$ , was determined directly from the 1D extracted spectra. We performed a least-squares fit to the gradient in the  $\ln(\lambda):\ln(f_\lambda)$  space, with the errors on  $\ln(f_\lambda)$  taken to be  $\ln(f_\lambda + \sigma) - \ln(f_\lambda)$  for each extracted spectral pixel (where  $\sigma$  is the noise). For all objects we fit the  $\beta$  slope over the rest-frame wavelength range 1250 – 2600 Å, following [45], with the exception of JADES-GS-z10-0 where we used a slightly smaller range of 1500 – 2600 Å to avoid the possible Ly $\alpha$  emission and damping wing. These results were also consistent with those from fitting a power-law to  $f_\lambda \propto \lambda^{-\beta}$  in linear wavelength space, weighting each point by  $1/\sigma^2$ .

We determined the absolute magnitude in the rest-frame UV ( $M_{UV}$ ) around  $\lambda_{rest} = 1500$  Å by measuring the average flux density per unit frequency interval ( $f_\nu$ ) from the extracted spectra over the rest-frame wavelength range 1400 – 1600 Å, and accounting for luminosity distance. The errors on each individual pixel flux density were combined in quadrature to derive the uncertainty in  $\beta$ .

We note that  $M_{UV}$  measured from the spectrum alone is somewhat fainter and the  $\beta$  somewhat redder for JADES-GS-z12-0 than that measured from NIRC*am* data in the companion paper[10]. We attribute this to remaining

slit-losses since this object is quite close to the edge of the shutter. This highlights the importance of the complementarity between NIRSpec spectroscopy and NIRCам photometry. Without the photometry we cannot correct for slit-losses when objects are large or off-centre, and so cannot report total SFRs or stellar masses of objects, even if other parameter estimation is only marginally affected. The difference is more stark for JADES-GS-z13-0 and so we report  $M_{\text{UV}}$  and  $\beta$  derived from SED modelling including the NIRCам photometry in this case (see Section 3). The comparison with the measurements in ref. [10] show good agreement for JADES-GS-z10-0 and JADES-GS-z11-0.

### 3 BEAGLE SED fitting

We perform full spectral fitting to the R100 spectra using the BEAGLE code [31]. In general, firm constraints on metallicities (both nebular and stellar) and gas parameters require the spectroscopic detection of emission and absorption lines, while constraints on total stellar masses and star-formation rates require NIRCам photometry, since NIRSpec MSA spectra are so prone to slit losses. Since these objects are so small [ $r_{1/2} \simeq 50 - 165$  kpc, with on-sky sizes of  $\theta_{1/2} \simeq 0.015 - 0.04''$  10] we use pre-calculated point-source slit-loss corrections. Therefore, in this paper we present an entirely independent analysis to that in ref. [10], both in data-sets used (excepting to the fits to JADES-GS-z13-0 where we employ the NIRCам photometry, see later in this section for details) and in SED codes and parameterizations. We comment on the consistency between the two analyses throughout this section.

This requires modelling of the wavelength-dependent line-spread function (LSF). We fit Gaussian profiles to emission lines in R100 spectra taken within this deep pointing and compare their widths as a function of wavelength to the dispersion curves provided by STScI\*. We find that the supplied dispersion curves multiplied by a factor of 0.7 provide a reasonable representation of the measured wavelength-dependent LSF.

We use spectra extracted over the full micro-shutter aperture to minimise the effects of wavelength dependent losses, since the size of the shutter is more than twice the width of the PSF at  $5\mu\text{m}$ . JADES-GS-z13-0, however, is just at the edge of the shutter and the 2D spectrum shows that it is clearly truncated. Therefore, to provide information of the aperture losses we use a 3-pixel extraction box to maximise S/N and simultaneously fit to the NIRCам aperture photometry [10]. We multiply the shape of the spectrum by a second-order polynomial, sampling over the polynomial coefficients in the fit. This essentially allows the NIRCам photometry to set the normalisation of the spectrum while also correcting wavelength-dependent slit-losses in the spectral calibration. The fits and associated parameter constraints are shown in Extended Data Figures 2-5. We note that SED fitting is performed in the companion paper [10], yet there they fit only to NIRCам photometry, fixing the redshift to

---

\*<https://jwst-docs.stsci.edu/jwst-near-infrared-spectrograph/nirspec-instrumentation/nirspec-dispersers-and-filters>

the spectroscopic redshift. Here we perform a complimentary analysis, fitting only to the spectra (except for JADES-GS-z13-0, as explained above).

For our BEAGLE fits, we mask the region of possible Ly $\alpha$  in JADES-GS-z10-0 (between 1.4148 and 1.4509 $\mu$ m, inclusive), since it is offset from the break, and would require specialised modelling of the line shape and offset to account for it properly. The masked region is shown as pale blue in the spectrum in Extended Data Figure 3. For JADES-GS-z12-0, we mask regions of rest-frame UV emission lines (light blue regions in Extended Data Figure 4 covering 2.1081 to 2.1620 $\mu$ m, 2.2875 to 2.3181 $\mu$ m and 2.6261 to 2.6533 $\mu$ m) since noise structure in the spectrum is over-fitted if left un-masked.

We then fit the spectra following the procedure of [46]. We use a constant SFH and fixed nebular parameters since we see no emission lines. The list of parameters employed in the fits, as well as priors set are given in Extended Data Table 2. We use the updated Bruzual & Charlot stellar population synthesis templates [47], as described in [48] with the physically consistent nebular line+continuum emission grid of [49]. We adopt a Chabrier [50] initial mass function with an upper mass limit of 100M $_{\odot}$ . We have verified that the results are not significantly changed when assuming an upper mass limit of 300M $_{\odot}$ . We account for the depletion of metals onto dust grains in the photoionized interiors of stellar birth clouds and include attenuation by dust in the outer neutral envelopes of the clouds and in the diffuse ISM [51]. We set the ionisation parameter,  $\log U_s$ , to be dependent on the nebular metallicity (and hence stellar metallicity) according to

$$\log U_s = -3.638 + 0.055Z + 0.68Z^2 \quad (1)$$

which follows the observations of [52]. The results do not change significantly for JADES-GS-z10-0 and JADES-GS-z11-0 when  $\log U_s$  is allowed to vary freely between  $-4 < \log U_s < -1$ . However, Z and  $\log U_s$  are unconstrained in JADES-GS-z13-0, and poorly constrained in JADES-GS-z12-0, when  $\log U_s$  is allowed to vary freely.

Since the constraints on the stellar metallicity are, at least in part, driven by the lack of strong emission lines, we tested whether recent cessation of star formation would significantly change the constraints. We therefore tested a constant star formation history where the SFR of the recent 10 Myr was allowed to vary independently (and decrease). We find that the star-formation rate,  $\Psi$ , is fairly unconstrained with low posterior median values, meaning recent cessation is consistent with the data. However, we still infer very low metallicities in JADES-GS-z10-0 and JADES-GS-z11-0 (the two with the highest S/N spectra). For the two lower S/N spectra (JADES-GS-z12-0 and JADES-GS-z13-0), Z,  $\hat{\tau}_v$  and  $\Psi$  are very poorly constrained when this extra free parameter is included. We show the results for JADES-GS-z10-0 and JADES-GS-z11-0 in Extended Data Table 3.

Another possibility to explain relatively weak line emission is a high escape of Lyman-continuum photons from the galaxy. We fit with a picket fence model



[where there are clear sight-lines to the stars through the nebular regions surrounding the birth clouds, 53]. The results are given in Extended Data Table 4 for the two objects (JADES-GS-z10-0 and JADES-GS-z11-0) with the highest S/N spectra. We note that JADES-GS-z10-0 shows a solution with very low age (a few Myr) and high escape fraction. The measured metallicity is marginally higher in this case, but still very low within the  $1\sigma$  credible interval. JADES-GS-z11-0 does not show such a peak in the posterior distribution function, with fits still favoring older ages and escape fractions which are essentially unconstrained (spanning the input uniform prior). We note that these results are consistent with ref. [10], who find similarly low age and high escape fraction for JADES-GS-z10-0 compared to JADES-GS-z11-0.

We also fit the spectra assuming the main feature is a Balmer break (see also Sec. 2). The results are shown in Extended Data Figure 6. Here, we fit a delayed SFH which halted a Gyr prior to observation, varying metallicity, maximum stellar age and redshift within a tight prior centred on the assumed redshift in the case that the break is a Balmer break. We see that the fits consistently fail to reproduce the peak and blue slope red-ward of the break, showing poor spectral fits. Additionally, JADES-GS-z10-0 and JADES-GS-z11-0 show flux blue-ward of the break in the fitted models which is clearly inconsistent with the measured flux and noise limits.

## 4 Damping wing profile

Galaxies at the very large redshifts presented in this paper are embedded in a largely neutral IGM, which has not yet undergone reionization. In this case the effective optical depth of the hydrogen at lower redshifts along the line sight becomes so large that the accumulated absorption in the Lorentzian scattering wing of the Lyman alpha resonance line causes intergalactic absorption to spill over into wavelengths above the rest frame Ly $\alpha$  line. This so-called damping wing absorption softens the sharp cutoff in the spectrum due to the intervening intergalactic hydrogen.

We have included the effect of the damping wing absorption in our spectral fits using the prescription presented by Miralda-Escudé [54], who first pointed out the important effect. The model assumes that the damping wing arises in a uniformly distributed completely neutral IGM containing the bulk of the baryons in the universe. For a source at a given redshift  $z_s$  it has only two free parameters,  $\tau_0$ , the overall strength of the Lyman alpha absorption in the form of the optical depth of the classical Gunn-Peterson trough [55] at a reference redshift of  $z = 5$ , and  $z_n$ , the redshift below which the intergalactic hydrogen is assumed to abruptly transition from fully neutral to fully ionized.

These two parameters are in turn set by the assumed cosmological model, which we here take to be Planck 2015  $\Lambda$ CDM [56]. This model's baryonic density parameter of  $\Omega_b h = 0.033$ , total mass density parameter  $\Omega_M = 0.309$ , together with the primordial Helium abundance of  $Y = 24\%$  translate into  $\tau_0 = 3.1 \times 10^5$ . The Planck satellite also measured  $z_n = 8.8$  for this cosmology,

although the predicted damping wing absorption is insensitive to this parameter at the large  $z > 10$  redshifts relevant here. A partially reionized IGM is included in the customary manner by multiplying  $\tau_0$  by the volume-averaged neutral fraction  $x_{\text{HI}}$ . This simple model ignores the potential complications of the galaxies being observed displaying strong intrinsic neutral hydrogen absorption, or their having already reionized a large volume of their immediate surroundings [57].

**Data availability** The data that support the findings of this study are available from the corresponding author upon reasonable request.

**Code availability** BEAGLE is available via a Docker image (distributed through docker hub) upon request at <https://iap.fr/beagle>.

**Acknowledgments.** ECL acknowledges support of an STFC Webb Fellowship (ST/W001438/1). SC acknowledges support by European Union’s HE ERC Starting Grant No. 101040227 - WINGS. MC, FDE, TJJ, RM, JW, and LS acknowledge support by the Science and Technology Facilities Council (STFC), ERC Advanced Grant 695671 “QUENCH”. RM is further supported by a research professorship from the Royal Society. JW is further supported by the Fondation MERAC. HÜ gratefully acknowledges support by the Isaac Newton Trust and by the Kavli Foundation through a Newton-Kavli Junior Fellowship. NB and PJ acknowledge support from the Cosmic Dawn Center (DAWN), funded by the Danish National Research Foundation under grant no.140. RS acknowledges support from a STFC Ernest Rutherford Fellowship (ST/S004831/1). AJB, AJC, JC, IEBW, AS, & GCJ acknowledge funding from the “FirstGalaxies” Advanced Grant from the European Research Council (ERC) under the European Union’s Horizon 2020 research and innovation programme (Grant agreement No. 789056). BER, BDJ, DJE, MR, EE, GR, CNAW, and FS acknowledge support from the JWST/NIRCam Science Team contract to the University of Arizona, NAS5-02015. DJE is further supported as a Simons Investigator. RB acknowledges support from an STFC Ernest Rutherford Fellowship [grant number ST/T003596/1]. REH acknowledges support from the National Science Foundation Graduate Research Fellowship Program under Grant No. DGE-1746060. SAR, BRP, and MP acknowledge support from the research project PID2021-127718NB-I00 of the Spanish Ministry of Science and Innovation/State Agency of Research (MICIN/AEI). MP is further supported by the Programa Atracción de Talento de la Comunidad de Madrid via grant 2018-T2/TIC-11715. LW acknowledges support from the National Science Foundation Graduate Research Fellowship under Grant No. DGE-2137419. KB is supported in part by the Australian Research Council Centre of Excellence for All Sky Astrophysics in 3 Dimensions (ASTRO 3D), through project number CE170100013. RH was funded by the Johns Hopkins University, Institute for Data Intensive Engineering and Science (IDIES). This research made use of the lux supercomputer at UC Santa Cruz, funded by NSF MRI grant AST 1828315. Acknowledgement for getting assigned a protected node for the DEEP BagPipes runs: "This study made use of the Prospero high performance computing facility at Liverpool John Moores University."

**Author contributions.** ECL and SCa led the writing of this paper. MR, CNAW, EE, FS, KH, CCW contributed to the design, construction, and commissioning of NIRCам. AB, AD, CNAW, CW, DJE, H-WR, MR, PF, PJ, RM, SA1, SAr contributed to the design of the JADES survey. BER, ST, BDJ, CNAW, DJE, IS, MR, RE, ZC contributed to the JADES imaging data reduction. RHa, BER contributed to the JADES imaging data visualization. BDJ, ST, AD, DPS, LW, MWT, RE contributed the modeling of galaxy photometry. KH, JMH, JL, LW, RE, REH contributed the photometric redshift determination and target selection. BDJ, EN, KAS, ZC contributed to the JADES imaging morphological analysis. BER, CNAW, CCW, KH, MR contributed to the JADES pre-flight imaging data challenges. SCa, MC, JW, PF, GG, SAr, BRdP, contributed to the NIRSpec data reduction and to the development of the NIRSpec pipeline PJ, NB, SAr contributed to the design and optimisation of the MSA configurations. AJC, AB, CNAW, ECL, HU, RB, KB, contributed to the selection, prioritisation and visual inspection of the targets. Sch, JC, ECL, RM, JW, RS, FDE, MM, MC, AdG, GJ, AS, LS contributed to analysis of the spectroscopic data, including redshift determination and spectral modelling. PJ, PF, MS, TR, GG, NL, NK, BRdP contributed to the design, construction and commissioning of NIRSpec. FDE, TL, MM, MC, BRdP, RM, SAr contributed to the development of the tools for the spectroscopic data analysis, visualisation and fitting. CW contributed to the design of the spectroscopic observations and MSA configurations. BER, CW, DJE, DPS, MR, NL, and RM serve as the JADES Steering Committee.

## References

- [1] Dayal, P., Ferrara, A.: Early galaxy formation and its large-scale effects. *Physics Reports* **780**, 1–64 (2018) <https://arxiv.org/abs/1809.09136> [astro-ph.GA]. <https://doi.org/10.1016/j.physrep.2018.10.002>
- [2] Donnan, C.T., et al.: The evolution of the galaxy UV luminosity function at redshifts  $z \sim 8$ –15 from deep JWST and ground-based near-infrared imaging. *arXiv e-prints*, 2207–12356 (2022) <https://arxiv.org/abs/2207.12356> [astro-ph.GA]
- [3] Harikane, Y., *et al.*: A Search for H-Dropout Lyman Break Galaxies at  $z$  12–16. *Astrophys. J.* **929**(1), 1 (2022) <https://arxiv.org/abs/2112.09141> [astro-ph.GA]. <https://doi.org/10.3847/1538-4357/ac53a9>
- [4] Adams, N.J., et al.: Discovery and properties of ultra-high redshift galaxies ( $9 < z < 12$ ) in the JWST ERO SMACS 0723 Field. *arXiv e-prints*, 2207–11217 (2022) <https://arxiv.org/abs/2207.11217> [astro-ph.GA]
- [5] Finkelstein, S.L., et al.: CEERS Key Paper I: An Early Look into the First 500 Myr of Galaxy Formation with JWST. *arXiv e-prints*, 2211–05792 (2022) <https://arxiv.org/abs/2211.05792> [astro-ph.GA]

- [6] Finkelstein, S.L., et al.: A Long Time Ago in a Galaxy Far, Far Away: A Candidate  $z \sim 12$  Galaxy in Early JWST CEERS Imaging. arXiv e-prints, 2207–12474 (2022) <https://arxiv.org/abs/2207.12474> [astro-ph.GA]
- [7] Castellano, M., *et al.*: Early Results from GLASS-JWST. III. Galaxy Candidates at  $z$  9–15. *Astrophys. J. Lett.* **938**(2), 15 (2022) <https://arxiv.org/abs/2207.09436> [astro-ph.GA]. <https://doi.org/10.3847/2041-8213/ac94d0>
- [8] Whitler, L., et al.: On the ages of bright galaxies  $\sim 500$  Myr after the Big Bang: insights into star formation activity at *zrsim15* with JWST. arXiv e-prints, 2208–01599 (2022) <https://arxiv.org/abs/2208.01599> [astro-ph.GA]
- [9] Atek, H., et al.: Revealing Galaxy Candidates out to  $z \sim 16$  with JWST Observations of the Lensing Cluster SMACS0723. arXiv e-prints, 2207–12338 (2022) <https://arxiv.org/abs/2207.12338> [astro-ph.GA]
- [10] Robertson, B.E., et al.: Discovery and properties of the earliest galaxies with confirmed distances. submitted to Nature (2022)
- [11] Bromm, V., Coppi, P.S., Larson, R.B.: The Formation of the First Stars. I. The Primordial Star-forming Cloud. *Astrophys. J.* **564**(1), 23–51 (2002) <https://arxiv.org/abs/astro-ph/0102503> [astro-ph]. <https://doi.org/10.1086/323947>
- [12] Schneider, R., Ferrara, A., Salvaterra, R.: Dust formation in very massive primordial supernovae. *Mon. Not. R. Astron. Soc.* **351**(4), 1379–1386 (2004) <https://arxiv.org/abs/astro-ph/0307087> [astro-ph]. <https://doi.org/10.1111/j.1365-2966.2004.07876.x>
- [13] Jeon, M., Bromm, V., Pawlik, A.H., Milosavljević, M.: The first galaxies: simulating their feedback-regulated assembly. *Mon. Not. R. Astron. Soc.* **452**(2), 1152–1170 (2015) <https://arxiv.org/abs/1501.01002> [astro-ph.GA]. <https://doi.org/10.1093/mnras/stv1353>
- [14] Vogelsberger, M., *et al.*: High-redshift JWST predictions from IllustrisTNG: dust modelling and galaxy luminosity functions. *Mon. Not. R. Astron. Soc.* **492**(4), 5167–5201 (2020) <https://arxiv.org/abs/1904.07238> [astro-ph.GA]. <https://doi.org/10.1093/mnras/staa137>
- [15] Hutter, A., *et al.*: Astraeus I: the interplay between galaxy formation and reionization. *Mon. Not. R. Astron. Soc.* **503**(3), 3698–3723 (2021) <https://arxiv.org/abs/2004.08401> [astro-ph.GA]. <https://doi.org/10.1093/mnras/stab602>
- [16] Wilkins, S.M., et al.: First Light And Reionisation Epoch Simulations

- (FLARES) V: The redshift frontier. arXiv e-prints, 2204–09431 (2022) <https://arxiv.org/abs/2204.09431> [astro-ph.GA]
- [17] Steidel, C.C., Giavalisco, M., Pettini, M., Dickinson, M., Adelberger, K.L.: Spectroscopic Confirmation of a Population of Normal Star-forming Galaxies at Redshifts  $Z > 3$ . *Astrophys. J. Lett.* **462**, 17 (1996) <https://arxiv.org/abs/astro-ph/9602024> [astro-ph]. <https://doi.org/10.1086/310029>
- [18] Madau, P., *et al.*: High-redshift galaxies in the Hubble Deep Field: colour selection and star formation history to  $z \sim 4$ . *Mon. Not. R. Astron. Soc.* **283**(4), 1388–1404 (1996) <https://arxiv.org/abs/astro-ph/9607172> [astro-ph]. <https://doi.org/10.1093/mnras/283.4.1388>
- [19] Steidel, C.C., *et al.*: Lyman Break Galaxies at Redshift  $z \sim 3$ : Survey Description and Full Data Set. *Astrophys. J.* **592**(2), 728–754 (2003) <https://arxiv.org/abs/astro-ph/0305378> [astro-ph]. <https://doi.org/10.1086/375772>
- [20] Zavala, J.A., *et al.*: A dusty starburst masquerading as an ultra-high redshift galaxy in JWST CEERS observations. arXiv e-prints, 2208–01816 (2022) <https://arxiv.org/abs/2208.01816> [astro-ph.GA]
- [21] Jakobsen, P., *et al.*: The Near-Infrared Spectrograph (NIRSpec) on the James Webb Space Telescope. I. Overview of the instrument and its capabilities. *Astron. Astrophys.* **661**, 80 (2022) <https://arxiv.org/abs/2202.03305> [astro-ph.IM]. <https://doi.org/10.1051/0004-6361/202142663>
- [22] Rieke, M.J., Kelly, D., Horner, S.: Overview of James Webb Space Telescope and NIRCам’s Role. *Proc. SPIE* **5904**, 1–8 (2005). <https://doi.org/10.1117/12.615554>
- [23] Bouwens, R.J., *et al.*: A candidate redshift  $z \sim 10$  galaxy and rapid changes in that population at an age of 500 Myr. *Nature* **469**(7331), 504–507 (2011) <https://arxiv.org/abs/0912.4263> [astro-ph.CO]. <https://doi.org/10.1038/nature09717>
- [24] Ellis, R.S., *et al.*: The Abundance of Star-forming Galaxies in the Redshift Range 8.5–12: New Results from the 2012 Hubble Ultra Deep Field Campaign. *Astrophys. J. Lett.* **763**(1), 7 (2013) <https://arxiv.org/abs/1211.6804> [astro-ph.CO]. <https://doi.org/10.1088/2041-8205/763/1/L7>
- [25] Koekemoer, A.M., *et al.*: The 2012 Hubble Ultra Deep Field (UDF12): Observational Overview. *Astrophys. J. Suppl. Ser.* **209**(1), 3 (2013) <https://arxiv.org/abs/1212.1448> [astro-ph.CO]. <https://doi.org/10.1088/0067-0049/209/1/3>

- [26] Brammer, G.B., *et al.*: A Tentative Detection of an Emission Line at 1.6  $\mu\text{m}$  for the  $z \sim 12$  Candidate UDFj-39546284. *Astrophys. J. Lett.* **765**(1), 2 (2013) <https://arxiv.org/abs/1301.0317> [astro-ph.CO]. <https://doi.org/10.1088/2041-8205/765/1/L2>
- [27] Bouwens, R.J., *et al.*: Evolution of the UV LF from  $z \sim 15$  to  $z \sim 8$  Using New JWST NIRC*am* Medium-Band Observations over the HUDF/XDF. arXiv e-prints, 2211–02607 (2022) <https://arxiv.org/abs/2211.02607> [astro-ph.GA]
- [28] Senchyna, P., *et al.*: Ultraviolet spectra of extreme nearby star-forming regions - approaching a local reference sample for JWST. *Mon. Not. R. Astron. Soc.* **472**(3), 2608–2632 (2017) <https://arxiv.org/abs/1706.00881> [astro-ph.GA]. <https://doi.org/10.1093/mnras/stx2059>
- [29] Senchyna, P., *et al.*: Extremely metal-poor galaxies with HST/COS: laboratories for models of low-metallicity massive stars and high-redshift galaxies. *Mon. Not. R. Astron. Soc.* **488**(3), 3492–3506 (2019) <https://arxiv.org/abs/1904.01615> [astro-ph.GA]. <https://doi.org/10.1093/mnras/stz1907>
- [30] Nanayakkara, T., *et al.*: Exploring He II  $\lambda 1640$  emission line properties at  $z \sim 2\text{--}4$ . *Astron. Astrophys.* **624**, 89 (2019) <https://arxiv.org/abs/1902.05960> [astro-ph.GA]. <https://doi.org/10.1051/0004-6361/201834565>
- [31] Chevallard, J., Charlot, S.: Modelling and interpreting spectral energy distributions of galaxies with BEAGLE. *Mon. Not. R. Astron. Soc.* **462**(2), 1415–1443 (2016) <https://arxiv.org/abs/1603.03037> [astro-ph.GA]. <https://doi.org/10.1093/mnras/stw1756>
- [32] Hirashita, H., Il'in, V.B., Pagani, L., Lefèvre, C.: Evolution of dust porosity through coagulation and shattering in the interstellar medium. *Mon. Not. R. Astron. Soc.* **502**(1), 15–31 (2021) <https://arxiv.org/abs/2101.02365> [astro-ph.GA]. <https://doi.org/10.1093/mnras/staa4018>
- [33] Chevallard, J., *et al.*: Physical properties and H-ionizing-photon production rates of extreme nearby star-forming regions. *Mon. Not. R. Astron. Soc.* **479**(3), 3264–3273 (2018) <https://arxiv.org/abs/1709.03503> [astro-ph.GA]. <https://doi.org/10.1093/mnras/sty1461>
- [34] Cullen, F., *et al.*: The ultraviolet continuum slopes ( $\beta$ ) of galaxies at  $z \simeq 8\text{--}15$  from JWST and ground-based near-infrared imaging. arXiv e-prints, 2208–04914 (2022) <https://arxiv.org/abs/2208.04914> [astro-ph.GA]
- [35] Topping, M.W., *et al.*: Searching for Extremely Blue UV Continuum Slopes at  $z = 7\text{--}11$  in JWST/NIRC*am* Imaging: Implications for Stellar

- Metallicity and Ionizing Photon Escape in Early Galaxies. arXiv e-prints, 2208–01610 (2022) <https://arxiv.org/abs/2208.01610> [astro-ph.GA]
- [36] Bouwens, R.J., *et al.*: Very Blue UV-Continuum Slope  $\beta$  of Low Luminosity  $z \sim 7$  Galaxies from WFC3/IR: Evidence for Extremely Low Metallicities? *Astrophys. J. Lett.* **708**(2), 69–73 (2010) <https://arxiv.org/abs/0910.0001> [astro-ph.CO]. <https://doi.org/10.1088/2041-8205/708/2/L69>
- [37] Endsley, R., *et al.*: A JWST/NIRCam Study of Key Contributors to Reionization: The Star-forming and Ionizing Properties of UV-faint  $z \sim 7 - 8$  Galaxies. arXiv e-prints, 2208–14999 (2022) <https://arxiv.org/abs/2208.14999> [astro-ph.GA]
- [38] Greig, B., *et al.*: IGM damping wing constraints on reionization from covariance reconstruction of two  $z \gtrsim 7$  QSOs. *Mon. Not. R. Astron. Soc.* **512**(4), 5390–5403 (2022) <https://arxiv.org/abs/2112.04091> [astro-ph.CO]. <https://doi.org/10.1093/mnras/stac825>
- [39] Davies, F.B., *et al.*: Predicting Quasar Continua near Ly $\alpha$  with Principal Component Analysis. *Astrophys. J.* **864**(2), 143 (2018) <https://arxiv.org/abs/1801.07679> [astro-ph.GA]. <https://doi.org/10.3847/1538-4357/aad7f8>
- [40] Ferruit, P., *et al.*: The Near-Infrared Spectrograph (NIRSpec) on the James Webb Space Telescope. II. Multi-object spectroscopy (MOS). *Astron. Astrophys.* **661**, 81 (2022) <https://arxiv.org/abs/2202.03306> [astro-ph.IM]. <https://doi.org/10.1051/0004-6361/202142673>
- [41] Birkmann, S.M., *et al.*: Wavelength calibration of the JWST near-infrared spectrograph (NIRSpec). *Proc. SPIE* **8150**, 81500 (2011). <https://doi.org/10.1117/12.893896>
- [42] Böker, T., *et al.*: The spectro-photometric calibration of the JWST NIRSpec instrument. *Proc. SPIE* **8442**, 84423 (2012). <https://doi.org/10.1117/12.925369>
- [43] Giardino, G., *et al.*: The Impact of Cosmic Rays on the Sensitivity of JWST/NIRSpec. *Publ. Astron. Soc. Pac.* **131**(1003), 094503 (2019) <https://arxiv.org/abs/1907.04051> [astro-ph.IM]. <https://doi.org/10.1088/1538-3873/ab2fd6>
- [44] Kriek, M., *et al.*: Direct Measurements of the Stellar Continua and Balmer/4000 Å Breaks of Red  $z > 2$  Galaxies: Redshifts and Improved Constraints on Stellar Populations I. *Astrophys. J.* **645**(1), 44–54 (2006) <https://arxiv.org/abs/astro-ph/0603063> [astro-ph]. <https://doi.org/10.1086/504103>

- [45] Calzetti, D., Kinney, A.L., Storchi-Bergmann, T.: Dust Extinction of the Stellar Continua in Starburst Galaxies: The Ultraviolet and Optical Extinction Law. *Astrophys. J.* **429**, 582 (1994). <https://doi.org/10.1086/174346>
- [46] Chevillard, J., *et al.*: Simulating and interpreting deep observations in the Hubble Ultra Deep Field with the JWST/NIRSpec low-resolution ‘prism’. *Mon. Not. R. Astron. Soc.* **483**(2), 2621–2640 (2019) <https://arxiv.org/abs/1711.07481> [astro-ph.GA]. <https://doi.org/10.1093/mnras/sty2426>
- [47] Bruzual, G., Charlot, S.: Stellar population synthesis at the resolution of 2003. *Mon. Not. R. Astron. Soc.* **344**(4), 1000–1028 (2003) <https://arxiv.org/abs/astro-ph/0309134> [astro-ph]. <https://doi.org/10.1046/j.1365-8711.2003.06897.x>
- [48] Vidal-García, A., Charlot, S., Bruzual, G., Hubeny, I.: Modelling ultraviolet-line diagnostics of stars, the ionized and the neutral interstellar medium in star-forming galaxies. *Mon. Not. R. Astron. Soc.* **470**(3), 3532–3556 (2017) <https://arxiv.org/abs/1705.10320> [astro-ph.GA]. <https://doi.org/10.1093/mnras/stx1324>
- [49] Gutkin, J., Charlot, S., Bruzual, G.: Modelling the nebular emission from primeval to present-day star-forming galaxies. *Mon. Not. R. Astron. Soc.* **462**(2), 1757–1774 (2016) <https://arxiv.org/abs/1607.06086> [astro-ph.GA]. <https://doi.org/10.1093/mnras/stw1716>
- [50] Chabrier, G.: Galactic Stellar and Substellar Initial Mass Function. *Publ. Astron. Soc. Pac.* **115**(809), 763–795 (2003) <https://arxiv.org/abs/astro-ph/0304382> [astro-ph]. <https://doi.org/10.1086/376392>
- [51] Charlot, S., Fall, S.M.: A Simple Model for the Absorption of Starlight by Dust in Galaxies. *Astrophys. J.* **539**(2), 718–731 (2000) <https://arxiv.org/abs/astro-ph/0003128> [astro-ph]. <https://doi.org/10.1086/309250>
- [52] Carton, D., *et al.*: Inferring gas-phase metallicity gradients of galaxies at the seeing limit: a forward modelling approach. *Mon. Not. R. Astron. Soc.* **468**(2), 2140–2163 (2017) <https://arxiv.org/abs/1703.01090> [astro-ph.GA]. <https://doi.org/10.1093/mnras/stx545>
- [53] Heckman, T.M., *et al.*: Extreme Feedback and the Epoch of Reionization: Clues in the Local Universe. *Astrophys. J.* **730**(1), 5 (2011) <https://arxiv.org/abs/1101.4219> [astro-ph.CO]. <https://doi.org/10.1088/0004-637X/730/1/5>
- [54] Miralda-Escudé, J.: Reionization of the Intergalactic Medium and the Damping Wing of the Gunn–Peterson Trough. *Astrophys. J.* **501**(1), 15–22 (1998) <https://arxiv.org/abs/astro-ph/9708253> [astro-ph]. <https://doi.org/10.1086/309250>



[org/10.1086/305799](https://doi.org/10.1086/305799)

- [55] Gunn, J.E., Peterson, B.A.: On the Density of Neutral Hydrogen in Inter-galactic Space. *Astrophys. J.* **142**, 1633–1636 (1965). <https://doi.org/10.1086/148444>
- [56] Planck Collaboration, *et al.*: Planck 2015 results. XIII. Cosmological parameters. *Astron. Astrophys.* **594**, 13 (2016) <https://arxiv.org/abs/1502.01589> [astro-ph.CO]. <https://doi.org/10.1051/0004-6361/201525830>
- [57] McQuinn, M., Lidz, A., Zaldarriaga, M., Hernquist, L., Dutta, S.: Probing the neutral fraction of the IGM with GRBs during the epoch of reionization. *Mon. Not. R. Astron. Soc.* **388**(3), 1101–1110 (2008) <https://arxiv.org/abs/0710.1018> [astro-ph]. <https://doi.org/10.1111/j.1365-2966.2008.13271.x>

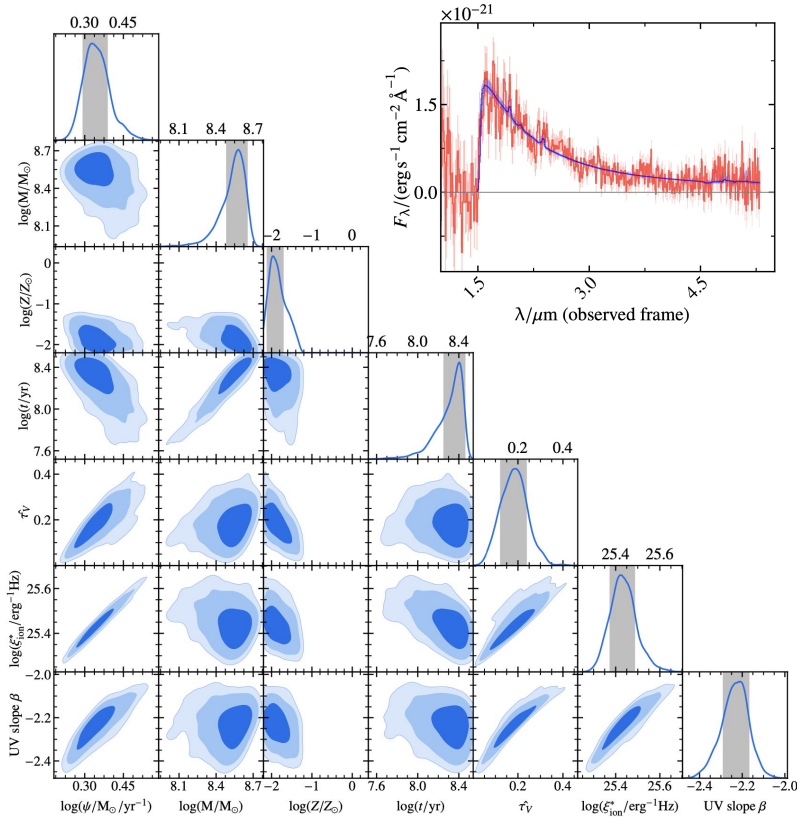
Extended Data Table 2	Parameter	Description	prior distributions used in BEAGLE	fitting
	Parameter	Description	Prior	
	$\log(M_{\text{tot}}/M_{\odot})$	Logarithm of the integrated SFH.	Uniform $\in [6, 12]$	
	$M/M_{\odot}$	Stellar mass, including stellar remnants.	Not fitted (dependent on $M_{\text{tot}}$ , $Z$ and $t$ )	
	$\psi/M_{\odot}\text{yr}^{-1}$	Current star formation rate.	Not fitted (dependent on $M_{\text{tot}}$ and $t$ )	
	$\log(Z/Z_{\odot})$	Logarithm of metallicity of stars.	Uniform $\in [-2.2, 0.4]$	
	$\log(Z_{\text{gas}}^{\text{HI}}/Z_{\odot})$	Metallicity of gas in H II.	Set equal to $Z$	
	$\hat{\tau}_{\text{V}}$	Total $V$ -band attenuation optical depth in the interstellar medium (ISM).	Exponential $\in [0, 6]$	
	$\mu$	Fraction of $\hat{\tau}_{\text{V}}$ arising from dust in the diffuse ISM	Fixed to 0.4.	
	$\log U_{\text{s}}$	Effective gas ionization parameter in H II regions	Dependent on $Z_{\text{gas}}^{\text{HI}}$ (following Eq. 1)	
	$\xi_{\text{d}}$	Dust-to-metal mass ratio in H II regions.	Fixed to 0.1	
	$n_{\text{H}}/\text{cm}^{-3}$ , $n_{\text{H}}^{\text{NLR}}/\text{cm}^{-3}$	Hydrogen gas density in H II regions	Fixed to 100.	
	$(\text{C/O})/(\text{C/O})_{\odot}$	Carbon-to-oxygen abundance ratio in units of $(\text{C/O})_{\odot} = 0.44$	Fixed to unity.	
	$m_{\text{up}}/M_{\odot}$	Upper mass cutoff of the IMF	Fixed to 100.	
	$\log(t/\text{Gyr})$	Logarithm of the age of the oldest stars.	Uniform $\in [6, 10.8]$	
	$z$	redshift	Gaussian $\mu_z = z_{1215}$ , $\sigma_z = 0.01$	

**Extended Data Table 3** | BEAGLE derived parameters when additionally fitting the star formation rate in the last 10 Myrs, which is allowed to vary freely independently of the previous history. We show the results when fitting to the two objects with highest S/N, JADES-GS-z10-0 and JADES-GS-z11-0 because the constraints on the other two objects are very poor when adding an extra free parameter to the fits.

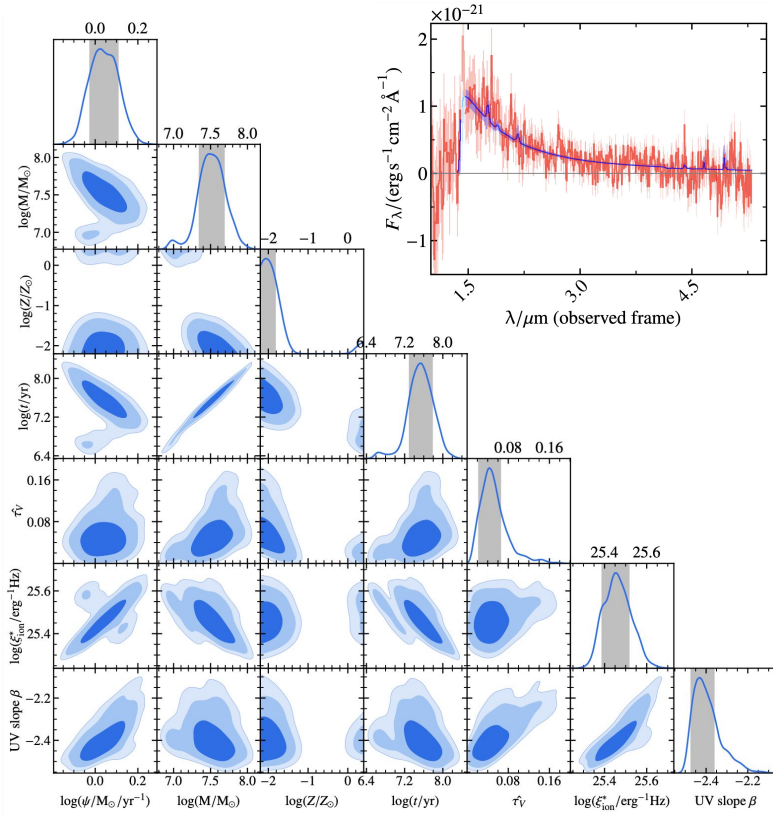
	JADES-GS-z10-0	JADES-GS-z11-0
$\log(M/M_{\odot})$	$7.8^{+0.12}_{-0.11}$	$8.85^{+0.12}_{-0.15}$
$\Psi/M_{\odot} \text{ yr}^{-1}$	$-2.11^{+1.28}_{-1.34}$	$-1.87^{+1.45}_{-1.37}$
$\log(t/\text{yr})$	$7.15^{+0.17}_{-0.11}$	$8.12^{+0.2}_{-0.28}$
$\log(Z/Z_{\odot})$	$-1.88^{+0.36}_{-0.21}$	$-1.87^{+0.33}_{-0.21}$
$\hat{\tau}_{\text{v}}$	$0.3^{+0.26}_{-0.18}$	$0.68^{+0.18}_{-0.2}$
$\xi_{\text{ion}}$	$25.04^{+0.17}_{-0.21}$	$24.73^{+0.25}_{-0.15}$

**Extended Data Table 4** | BEAGLE derived parameters when additionally fitting the escape fraction of Lyman-continuum photons,  $f_{\text{esc}}$ . We show the results when fitting to the two objects with highest S/N, JADES-GS-z10-0 and JADES-GS-z11-0 because the constraints on the other two objects are very poor when adding an extra free parameter to the fits.

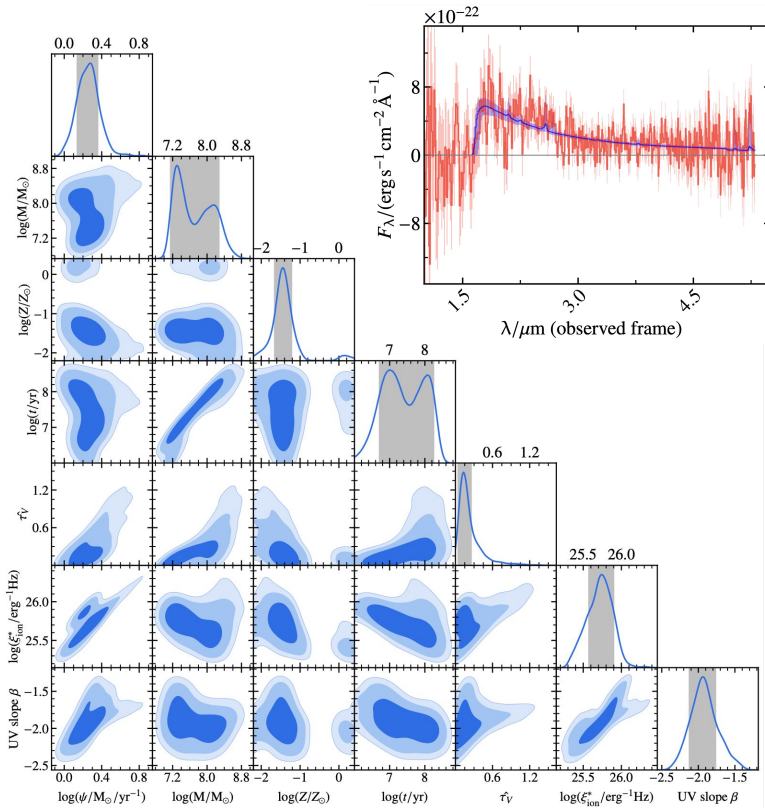
	JADES-GS-z10-0	JADES-GS-z11-0
$\log(M/M_{\odot})$	$7.41^{+0.1}_{-0.11}$	$8.7^{+0.11}_{-0.16}$
$\Psi/M_{\odot} \text{ yr}^{-1}$	$2.43^{+0.65}_{-0.58}$	$2.83^{+0.76}_{-0.47}$
$\log(t/\text{yr})$	$6.29^{+0.19}_{-0.2}$	$8.26^{+0.14}_{-0.23}$
$\log(Z/Z_{\odot})$	$-1.7^{+0.41}_{-0.33}$	$-1.8^{+0.29}_{-0.25}$
$\hat{\tau}_{\text{v}}$	$0.09^{+0.05}_{-0.04}$	$0.26^{+0.1}_{-0.08}$
$\xi_{\text{ion}}$	$26.01^{+0.12}_{-0.13}$	$25.54^{+0.12}_{-0.08}$
$f_{\text{esc}}$	$0.86^{+0.1}_{-0.13}$	$0.64^{+0.24}_{-0.32}$



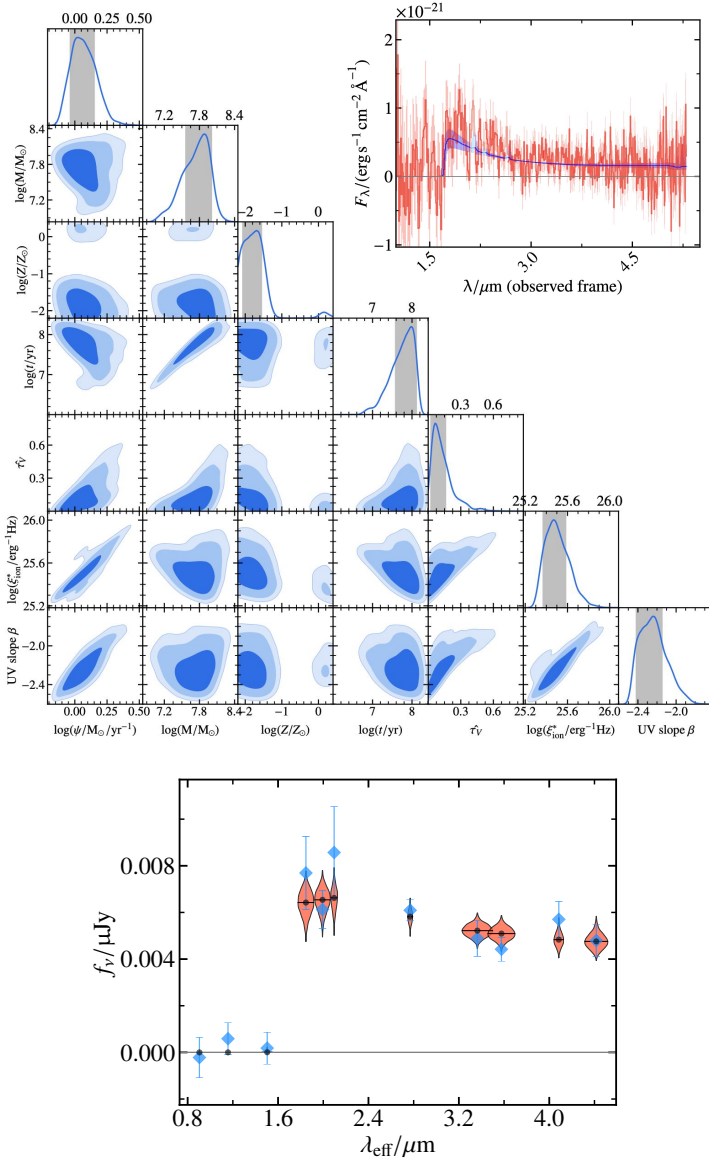
**Extended Data Fig. 2** | The results of full spectral fitting to JADES-GS-z11-0 with BEAGLE. We fit models to spectra extracted over the full shutter aperture to minimise the wavelength-dependent losses due to varying point-spread function (PSF). The triangle plot shows the 2D (off-diagonal) and 1D (along the main diagonal) posterior probability distributions on stellar mass ( $M$ ), metallicity ( $Z$ ), maximum age of stars ( $t$ ), effective dust attenuation optical depth in the V-band ( $\tau_V$ ), and redshift ( $z$ ) which are all derived from the BEAGLE fits. We also include the model constraints on the star-formation rate ( $\Psi$ ), UV slope ( $\beta$ ) and ionising photon emissivity ( $\xi_{\text{ion}}$ ), which are derived parameters of the model. The dark, medium and light blue contours show the extents of the 1, 2 and  $3\sigma$  credible regions of the posterior probability, respectively. The inset panel shows the observed spectrum and  $1\sigma$  uncertainties per pixel in red and light red respectively, and the  $1\sigma$  range in fitted model spectra in blue. We fit with a constant star formation history (more details in the text and section 3).



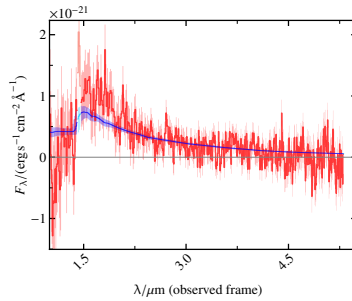
**Extended Data Fig. 3** | As for Extended Data Figure 2, but for BEAGLE fits to JADES-GS-z10-0.



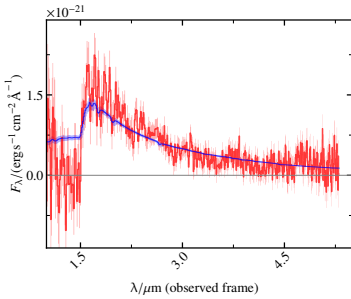
**Extended Data Fig. 4** | As for Extended Data Figure 2, but for BEAGLE fits to JADES-GS-z12-0.



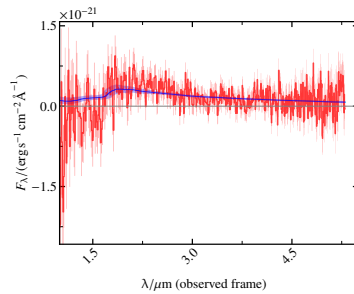
**Extended Data Fig. 5** | As for Extended Data Figure 2, but for BEAGLE fits to JADES-GS-z13-0(top panel). Bottom panel shows the observed photometry as blue diamonds and associated error-bars while the coral shaded regions show the model photometry in the same bands. Since this galaxy is very close to the edge of the shutter, we use an extraction over 3 pixels to maximise the S/N. Then to account for wavelength-dependent slit-losses we simultaneously fit the spectrum and NIRCcam photometry.



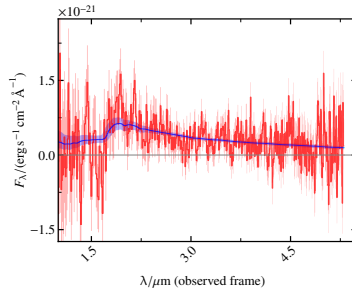
(c) JADES-GS-z10-0



(d) JADES-GS-z11-0



(e) JADES-GS-z12-0



(f) JADES-GS-z13-0

**Extended Data Fig. 6 | The fitted spectra if we force the observed spectral break to be interpreted as a Balmer break rather than a Lyman break.** We see that the fits fail to reproduce the blue slopes red-ward of the spectral break, and in the cases of JADES-GS-z10-0 and JADES-GS-z11-0, flux in the fitted models blue-ward of the break are significantly higher than the observed flux. Combined with the limits placed in section 2 (and presented in Table 1), these fits show that the observed spectra are inconsistent with being Balmer breaks.